ChemPubSoc Europe

DOI: 10.1002/chem.201801026

CHEMISTRY A European Journal Full Paper

Molecular Magnetism

A Pseudo-Octahedral Cobalt(II) Complex with Bispyrazolylpyridine Ligands Acting as a Zero-Field Single-Molecule Magnet with Easy Axis Anisotropy

Luca Rigamonti,*[a] Nathalie Bridonneau,[a, e] Giordano Poneti,[b, f] Lorenzo Tesi,[b] Lorenzo Sorace,[b] Dawid Pinkowicz,[c] Jesus Jover,[d] Eliseo Ruiz,[d] Roberta Sessoli,[b] and Andrea Cornia[a]

Abstract: The homoleptic mononuclear compound [Co(bpp-COOMe)$_2$](ClO$_4$)$_2$ (**1**) (bpp-COOMe = methyl 2,6-di(pyrazol-1-yl)pyridine-4-carboxylate) crystallizes in the monoclinic *C*2/*c* space group, and the cobalt(II) ion possesses a pseudo-octahedral environment given by the two *mer*-coordinated tridentate ligands. Direct-current magnetic data, single-crystal torque magnetometry, and EPR measurements disclosed the easy-axis nature of this cobalt(II) complex, which shows single-molecule magnet behavior when a static field is applied in alternating-current susceptibility measurements. Diamagnetic dilution in the zinc(II) analogue [Zn(bpp-COOMe)$_2$](ClO$_4$)$_2$ (**2**) afforded the derivative [Zn$_{0.95}$Co$_{0.05}$(bpp-COOMe)$_2$](ClO$_4$)$_2$ (**3**), which exhibits slow relaxation of magnetization even in zero field thanks to the reduction of dipolar interactions. Theoretical calculations confirmed the overall electronic structure and the magnetic scenario of the compound as drawn by experimental data, thus confirming the spin-phonon Raman relaxation mechanism, and a direct quantum tunneling in the ground state as the most plausible relaxation pathway in zero field.

Introduction

Single-molecule magnets (SMMs) can in principle be used for encoding binary information and for data processing, thus exploiting their magnetic bistability and inherent quantum behavior.[1] Research in this field moves in different directions, such as finding better performing systems,[2,3] developing reliable methods to deposit molecules on solid substrates,[4,5] and finding ways to control molecular magnetism by external stimuli, including light and pressure.[6–8] Complexes that contain only one metal center may represent the smallest chemically tuneable SMMs for spin-based devices,[9] and significant progress has been made in this regard by using lanthanides[3,10] and, more recently, 3d metal ions.[10,11] In the latter case, relaxation by quantum tunneling is usually very fast in zero field, so that application of a static field is required to observe SMM behavior by alternating-current (ac) susceptibility measurements. However, few examples of zero-field SMMs based on mononuclear complexes of iron(I)[12] iron(III),[13] and cobalt(II) have been reported,[14–25] which all feature half-integer spin states ($S = 3/2$ or 5/2). In particular, individual cobalt(II) ions were found to exhibit zero-field SMM behavior when embedded in tetrahedral,[14–17,20,22,24] trigonal prismatic,[18,19,23] or linear[21] coordination environments or in a solid-state lattice.[25] In all these cases, the metal complexes possess a negative zero field splitting (zfs) parameter (D), thus suggesting the investigation of other coordination environments suitable to enforce an easy-axis magnetic anisotropy on the cobalt(II) ion.

[a] Dr. L. Rigamonti, Dr. N. Bridonneau, Prof. A. Cornia
Dipartimento di Scienze Chimiche e Geologiche
Università degli Studi di Modena e Reggio Emilia
and INSTM RU of Modena and Reggio Emilia
via G. Campi 103, 41125 Modena (Italy)
E-mail: luca.rigamonti@unimore.it
luca.rigamonti@yahoo.com

[b] Dr. G. Poneti, Dr. L. Tesi, Prof. L. Sorace, Prof. R. Sessoli
Laboratory of Molecular Magnetism (LAMM), Dipartimento di Chimica 'Ugo Schiff', Università degli Studi di Firenze, and INSTM RU of Firenze
via della Lastruccia 3–13, 50019 Sesto Fiorentino, FI (Italy)

[c] Dr. D. Pinkowicz
Faculty of Chemistry, Jagiellonian University
Gronostajowa 2, 30-387 Kraków (Poland)

[d] Dr. J. Jover, Prof. E. Ruiz
Departament de Química Inorgànica i Orgànica,
Institut de Química Teòrica i Computacional
Universitat de Barcelona, Diagonal 645, 08028 Barcelona (Spain)

[e] Dr. N. Bridonneau
Current address:
Laboratoire Interfaces Traitements Organisation
et Dynamique des Systèmes (ITODYS), UMR 7086 CNRS
Université Paris 7 Diderot, Paris Bât. Lavoisier
15 rue Jean-Antoine de Baïf, 75205 Paris Cedex 13 (France)

[f] Dr. G. Poneti
Current address:
Instituto de Química, Universidade Federal do Rio de Janeiro
21941-909 Rio de Janeiro (Brazil)

Supporting information and the ORCID numbers for the authors of this article can be found under https://doi.org/10.1002/chem.201801026.

The 2,6-bis(pyrazol-1-yl)pyridine (bpp) class of ligands is well known for the promotion of spin-crossover (SCO) in octahedral iron(II) metal complexes.[26–28] These ligands can host both high-spin (HS) and low-spin (LS) iron(II) centers,[27] thus enabling spin-state modulation by temperature or application of light.[29,30] In some cases, the distortion of the octahedral geometry is so pronounced as to block the metal center in its HS state, as we recently found when using methyl 2,6-di(pyrazol-1-yl)pyridine-4-carboxylate (bpp-COOMe).[26] In particular, in the distorted molecular structure of $[Fe(bpp\text{-}COOMe)_2](ClO_4)_2$, the pseudo-octahedral coordination environment leads to a stabilization of the d_{xy} orbital relative to d_{xz} and d_{yz} (where *z* represents the *trans*-N{pyridyl}-Fe-N{pyridyl} direction and *x* and *y* represent the directions of the coordinated pyrazolyl nitrogen atoms).[26]

Such an orbital pattern is expected to produce an easy-axis anisotropy for cobalt(II), as sought for.[31] We have thus synthesized $[Co(bpp\text{-}COOMe)_2](ClO_4)_2$ (**1**) by reaction of cobalt(II) perchlorate with bpp-COOMe and found this compound to be isostructural to the iron(II) complex.[26] From the study of the magnetic properties of **1**, we discovered that it has an easy-axis anisotropy and shows SMM behavior under an applied external field. Magnetic dilution in the zinc(II) analogue $[Zn(bpp\text{-}COOMe)_2](ClO_4)_2$ (**2**) afforded $[Zn_{0.95}Co_{0.05}(bpp\text{-}COOMe)_2](ClO_4)_2$ (**3**), in which dipolar interactions are reduced and slow relaxation of the magnetization is detectable even in zero field. To the best of our knowledge, this finding discloses the first fully characterized pseudo-octahedral cobalt(II) complex with easy-axis anisotropy that acts as a zero-field SMM.[32] Herein, we present detailed and critical descriptions of the experimental data collected by direct-current (dc) and ac magnetic measurements, X-band electron paramagnetic resonance (EPR) spectroscopy, single-crystal cantilever torque magnetometry (CTM), and ab initio theoretical calculations in support for the magnetic properties of **1**.

Results and Discussion

Synthesis, crystallization, and molecular structures

The reaction of a suspension of bpp-COOMe in acetonitrile with $[M(ClO_4)_2]\cdot 6H_2O$ (M=Co, Zn; either as pure salts or in a mixture) at room temperature produced the immediate dissolution of the ligand and formation of a solution, which gave well-formed X-ray-quality crystals of **1** (light red), **2** (colorless), or **3** (very light orange) in good yield by vapour diffusion with diethyl ether. The crystals of the three compounds are air stable, belong to the monoclinic space group *C*2/*c*, and are isomorphous to the iron(II) derivative recently studied for its SCO properties (see Tables S1 and S2 in the Supporting Information for a comparison of the room-temperature unit-cell parameters).[26] X-ray diffraction data were collected at 295 and 161 K for **1** and at 120 K for **2** to determine the molecular structures, and the main bond lengths and angles obtained are reported in Table 1.

In all cases, the metal coordination environments show a pronounced distortion from a perfect octahedral geometry

Table 1. Main bond lengths [Å] and angles [°] of **1** (Co) and **2** (Zn).

	1 [T = 295 K]	**1** [T = 161 K]	**2** [T = 120 K]
M1–N1	2.142(2)	2.141(2)	2.1428(16)
M1–N14	2.148(2)	2.152(2)	2.2056(16)
M1–N15 (py)	2.082(2)	2.080(2)	2.1216(16)
N1-M1-N15	74.56(9)	74.73(8)	74.43(6)
N15-M1-N14	74.91(9)	74.93(8)	73.49(6)
N1-M1-N14 (ψ)	148.76(9)	148.99(8)	147.72(6)
N15-M1-N15′[a] (ϕ)	161.12(13)	161.45(8)	160.36(6)
θ[b]	81.21	81.59	82.92
Σ[c]	140.1	139.1	145.6
Θ[c]	445	444	457

[a] The N15′ atom is obtained from N15 through a twofold rotation. [b] Dihedral angle between the two ligands (the plane of each ligand was defined as the least-squares plane through its sixteen aromatic C/N atoms). [c] See ref. [28] for the definition. py = pyridine.

(see Figure 1 and Figure S1 in the Supporting Information). This finding is best outlined by the *trans*-N{pyridyl}-M-N{pyridyl} angle (ϕ) and the dihedral angle between the least squares (ls) planes of the two *mer*-coordinated ligands (θ), which lie far from the ideal values of 180 and 90°, respectively.[27] Although

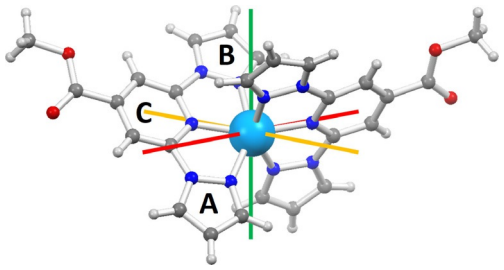

Figure 1. Molecular structure of the $[Co(bpp\text{-}COOMe)_2]^{2+}$ cation of **1** at low temperature in a perspective view with ring labeling (ring A = N1N4C3C2C1, ring B = N14N10C11C12C13, ring C = N15C5C6C7C8C9, where N1, N14, and N15 are the donor atoms to cobalt). The magnetic anisotropy axes were obtained by single-crystal CTM and EPR measurements. Co = azure, O = red, N = blue, C = light gray, H = white; easy axis = red, intermediate axis = green, hard axis = yellow.

the cobalt(II) ion in **1** is Jahn–Teller active,[33] the described distortion is most probably caused by crystal-packing effects because this distortion is present, to almost the same extent, in the zinc(II) derivative **2**. Note that the most regular geometry would still exhibit departures from the perfect octahedral symmetry due to the intrinsic shape of the bpp ligands, which imposes a clamp angle (ψ) of less than 180°. The distortion is also highlighted by the high values of the parameters Σ and Θ (Table 1). The first parameter is a general measure of the deviation of a metal ion from an ideal octahedral geometry, whereas the Θ value more specifically indicates the distortion from an octahedral environment toward a trigonal-prismatic structure.[28] In fact, a perfectly octahedral complex would give $\Sigma = \Theta = 0$.

The Co–N bond lengths in **1** (Table 1) range from 2.08 Å with the pyridyl nitrogen atom (ring C) to about 2.15 Å with

the pyrazolyl moieties (rings A and B), which are partially rotated by about 6–10° with respect to the ls plane of the whole ligand; furthermore, these values remain the same within experimental error upon variation of the temperature. The ester group is coplanar with the pyridyl ring C and is involved in one of the two shortest intermolecular interactions with one pyrazolyl C–H group (C1(H1)···O17 = 3.252/3.291 Å, C1-H1···O17 = 147.6/148.9° at 161/295 K), which leads to a Co···Co distance of 9.642/9.664 Å. The second short intermolecular contact involves another C–H group and the pyrazolyl ring of the adjacent molecule (C12(H12)···centroid(ring A) = 3.47/3.52 Å, C12-H12···centroid(ring A) = 150/149° at 161/295 K) with a shorter intermolecular Co···Co distance of 8.494/8.530 Å. Perchlorate anions are located in the voids between the cations, and all the oxygen atoms are involved in weak C–H···O interactions (see Figure S1 and Tables S3 and S4 in the Supporting Information).

The zinc derivative **2** shows similar structural features relative to **1**, with only slightly longer Zn–N distances with the pyrazolyl rings (Table 1), but fully comparable crystal packing (see Table S5 in the Supporting Information), which allowed us to successfully obtain the diamagnetically diluted crystalline sample **3** containing a Zn/Co ratio of 18:1 (i.e., $Zn_{0.9475}Co_{0.0525}$), as confirmed by inductively coupled plasma optical emission spectrometry (ICP-OES).

Static magnetic properties

Dc magnetic susceptibility data of **1** were recorded in the temperature range 2–300 K in a low-field regime (1 kOe up to 40 K and 10 kOe from 30 to 300 K), together with the field dependence of the isothermal molar magnetization (M_M) at low temperature (Figure 2). The product of the molar magnetic susceptibility (χ_M) and the temperature (T) was about 2.84 emu K mol^{-1} at 300 K, against an expected spin-only value of 1.875 emu K mol^{-1} for an $S = 3/2$ ion with $g = 2.00$. This difference indicates a relevant orbital contribution to the magnetism, which can be parametrized in the first approximation by

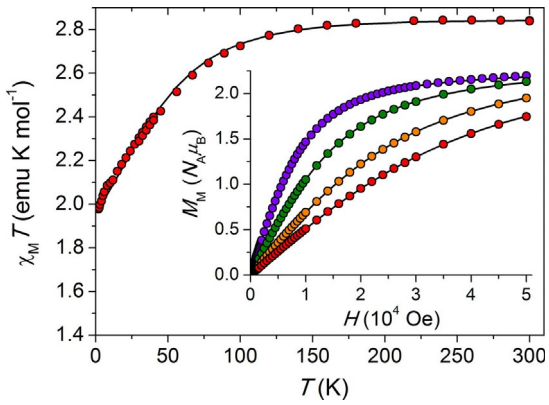

Figure 2. Temperature dependence of the $\chi_M T$ product for **1** (red circles in the main panel; overlapped points in the range 30–40 K refer to measurements at 1 and 10 kOe). Inset: field dependence of the molar magnetization (M_M) at 1.8 (blue), 3.0 (green), 5.0 (yellow), and 7.0 (red) K. Solid lines are given by the best-fit parameters (see the text for details).

assuming $g = 2.46$. The $\chi_M T$ value remains almost unvaried upon cooling down to 90 K, at which point it begins to slowly decrease to 1.98 emu K mol^{-1} at 2.0 K, which is consistent with the depopulation of the spin-orbit and low-symmetry split states of the $^4T_{1g}(O_h)$ electronic term.

Although a spin Hamiltonian formalism might be inadequate to account for the electronic structure of the cobalt(II) ion,[34] we first used the following Hamiltonian to fit the experimental $\chi_M T(T)$ and $M_M(H)$ data simultaneously by using the PHI program [Eq. (1)]:[35]

$$\begin{aligned}\mathcal{H} &= \mathcal{H}_{Zeeman} + \mathcal{H}_{zfs} = \mu_B \hat{B}\cdot\bar{\boldsymbol{g}}\cdot\hat{S} + \hat{S}\cdot\bar{\boldsymbol{D}}\cdot\hat{S} \\ &= g_x\mu_B B_x S_x + g_y\mu_B B_y S_y + g_z\mu_B B_z S_z + \\ &\quad D\left[S_z^2 - \frac{1}{3}S(S+1)\right] + E\left(S_x^2 - S_y^2\right)\end{aligned} \tag{1}$$

in which D and E are the axial and transverse second-order anisotropy parameters (defined from the principal components of the $\bar{\boldsymbol{D}}$ matrix as $D = 3D_{zz}/2$ and $E = (D_{xx} - D_{yy})/2$) and g_x, g_y, and g_z are the principal components of the $\bar{\boldsymbol{g}}$ matrix for the $S = 3/2$ state ($\bar{\boldsymbol{D}}$ and $\bar{\boldsymbol{g}}$ were assumed to be collinear). By taking an axial $\bar{\boldsymbol{g}}$ matrix with $g_x = g_y$ for simplicity, a systematic survey was performed with g_α values ($\alpha = x, y, z$) from 1.8 to 3.2 and diagonal components of $\bar{\boldsymbol{D}}$ from −90 to 90 cm^{-1}. An accurate fit was only possible for negative D values and a unique solution fulfilled the condition expected for easy-axis cobalt(II) ions, namely $g_z > g_x = g_y$: $D = -57.5(7)$, $|E| = 15.7(3)$ cm^{-1}; $g_x = g_y = 2.332(4)$, $g_z = 2.6687(15)$. As can be noted, the cobalt(II) ion has an easy-axis anisotropy, but with a relevant rhombic distortion, as given by $|E/D| = 0.273$ (the sign of E is irrelevant for powder measurements when $g_x = g_y$). The resulting splitting of the $S = 3/2$ manifold is $2(D^2 + 3E^2)^{1/2} = 127$ cm^{-1}.

Torque magnetometry

To gain independent experimental evidence of the magnetic anisotropy, CTM experiments were performed on a face-indexed single crystal of **1** mounted on a rotating capacitive cantilever torquemeter. The device measures the torque component (τ_Y) along the rotation axis (Y), whereas the magnetic field is applied normal to Y in the XZ plane at an angle θ from Z (θ increases going from Z toward $-X$).[36,37] The measured torque is thus given by Equation (2):

$$\tau_Y = m_Z B_X - m_X B_Z \tag{2}$$

in which $\mathbf{m} = (m_X, m_Y, m_Z)$ is the magnetic moment of the sample and $\mathbf{B} = (B_X, 0, B_Z)$ is the applied magnetic field. Two rotations (Rot1 and Rot2) were performed in which the XYZ frame corresponds to the orthogonalized crystallographic frame a^*bc (Rot1) or $-a^*cb$ (Rot2) (see the Supporting Information for further details). Thanks to the fact that the cobalt(II) ion in **1** is located on a binary axis of the monoclinic $C2/c$ space group, only one molecule is magnetically independent. Moreover, one of the principal directions of the magnetic anisotropy tensor (e.g., y) must coincide with this binary axis,

which is parallel to *b*, whereas the others (*x* and *z*) must lie in the *a***c* plane. When scanning this plane, as in Rot1, and working in the low-field limit Equation (2) becomes Equation (3):

$$\tau_y(\phi) = B^2(\chi_{zz}-\chi_{xx})\sin\phi\cos\phi \quad (3)$$

in which $\bar{\chi}$ is the susceptibility tensor and $\phi=\theta_z-\theta$ is the angle between the principal anisotropy axis *z* and **B** (i.e., the magnetic field is applied along *z* at $\theta=\theta_z$). The principal directions of the anisotropy tensor, separated by $\pi/2$ but arbitrarily located in the *a***c* plane, are easily detected as zero-torque points. Furthermore, the easy or hard character becomes evident by increasing the field at low temperature; as a result, when the low-field limit is no longer valid the curves become steeper around the hard-axis zero-torque point.[37] The measurements, performed at 10 K under a static magnetic field of 2 and 4 T and at 100 K with a magnetic field of 10 and 12 T, are reported in Figure 3, whereas the data at intermediate temperatures are available in Figure S2 (see the Supporting Information).

In Rot1 (*XYZ*=*a***bc*) at 10 K, we find the first torque zero point at $\theta=43^\circ$ on going from *c* toward $-a^*$; thus, the first in-plane principal direction (*x*) deviates by only about 10° from the *a* crystallographic axis (see Figure S3 in the Supporting Information). The second torque zero point occurs at $\theta=133^\circ$ and corresponds to the second in-plane principal direction *z* ($\theta_z=133^\circ$). The sign of the measured torque signal directly indicates that *z* (*x*) is the easy (hard) in-plane direction. The same conclusion can be reached looking at the data obtained at 4 T. At this field, the torque curve deviates from the simple angular dependence given by Equation (3), thus showing a steeper angular variation $\theta=43^\circ$, which is identified as the hard direction in the scanned plane.

For Rot2 (*XYZ*=−*a***cb*), the two torque zero points are found at $\theta=0$ and 90°, as expected; that is, when the field is applied along the *b* and *a** crystallographic axes, respectively. Unlike the former, the latter field orientation does not individuate a principal anisotropy axis, but only the projection on the *a***b* plane. Both the sign and shape of the torque signal in this rotation indicate that the crystal is more easily magnetized along *a** than *b*. However, it is not possible to establish whether *b* is the overall intermediate or hard anisotropy axis from a qualitative analysis. To solve this ambiguity, the data obtained at $T=10$ K were numerically simulated with the $S=3/2$ spin Hamiltonian in Equation (1). As a first step, the $\bar{\boldsymbol{g}}$ and $\bar{\boldsymbol{D}}$ matrices were constrained to have principal values determined by means of dc magnetic measurements, but the common principal directions were left free to reorient in space and an overall scale factor was refined to account for the incertitude on the mass of the crystal (ca. 80 μg). In a second step, the principal values were also left free to vary; however, this approach did not provide any improvement in the agreement.

In the end, the fitting procedure indicated that *b* is the overall intermediate axis (i.e., *y* in [Eq. (1)] with $E>0$), whereas the

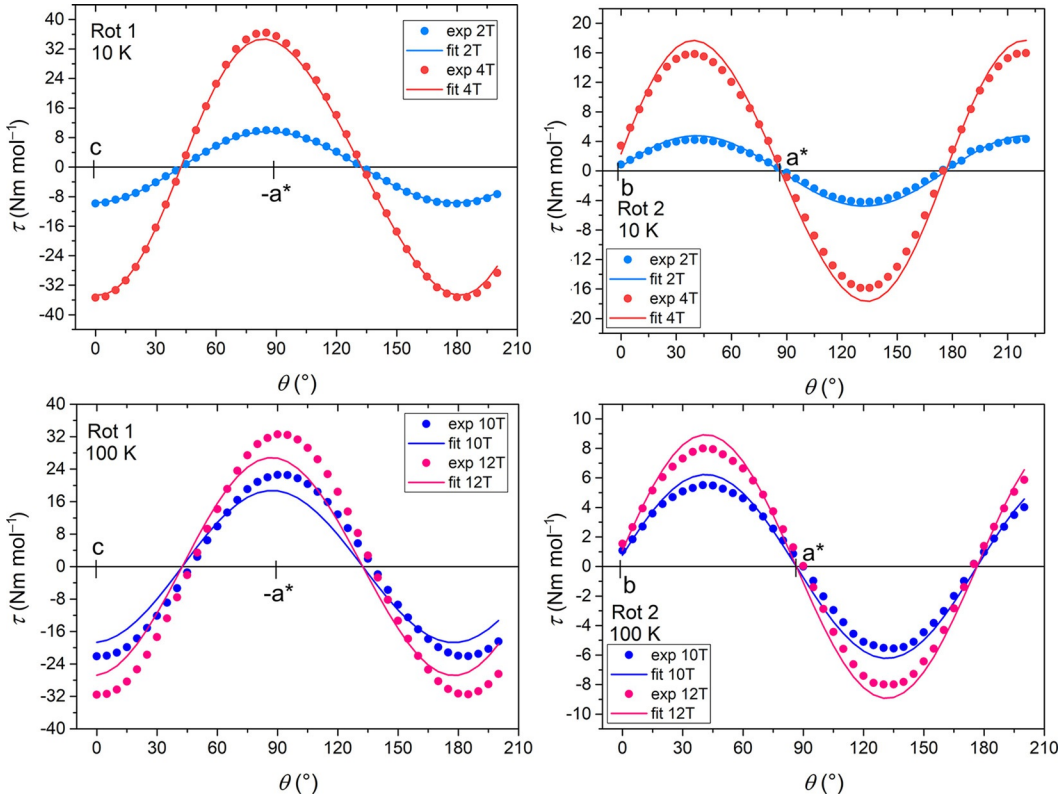

Figure 3. Experimental data (dots) and simulated curves with $S=3/2$ spin Hamiltonian (solid lines; N m mol^{-1}) of **1** obtained with CTM for two rotations at 10 and 100 K under different static magnetic fields. The common orientation of the $\bar{\boldsymbol{g}}$ and $\bar{\boldsymbol{D}}$ matrices was optimized from the 10 K data by using the principal values obtained from magnetization and susceptibility data.

*a***c* plane contains the easy (*z*) and hard (*x*) molecular magnetic axes, with the latter at approximately 10° from *a*. The orientation of the anisotropy axes shown in Figure 1 is superimposed onto the molecular structure, where the principal axes do not point toward, but between, the ligand atoms. The good agreement between the simulated and experimental torque data confirms the spin Hamiltonian parameters extracted from the static magnetic measurements, in particular the negative sign of *D* with a relatively large rhombicity. On the other hand, Figure 3 shows that the agreement is less satisfactory at 100 K. The inclusion of rhombicity in the $\bar{g}$ matrix (see the section on EPR spectroscopy), that is, $g_x \neq g_y$, does not improve the quality of the fit, as indeed expected because the torque measurements are mainly sensitive to the $\bar{D}$ tensor. Keeping in mind that the orbital angular momentum of the cobalt(II) ion may be not completely quenched, the magnetic properties are affected on increasing the temperature by spin-orbit coupled states at higher energies and the description of the metal ion as a simple $S=3/2$ spin may be no longer valid. This outcome would result in a failure of the spin Hamiltonian approach, thus leaving ab initio methods and explicit inclusion of the orbital contribution[34] as the only ways to appropriately describe the system (see below).

EPR spectroscopy

EPR spectroscopy can be regarded as a complementary technique to CTM because EPR spectroscopic analysis can easily provide detailed information on the $\bar{g}$ matrix. Low-temperature continuous-wave X-band EPR spectra were recorded for powder and single-crystal samples. The experimental spectrum of a powder sample of **3** (Figure 4) can be easily interpreted as arising from an effective spin doublet with strongly anisotropic *g* factor and hyperfine coupling with the nuclear spin $I=7/2$ of ^{59}Co (natural abundance = 100%). Similar spectra were obtained for **1**, although dominant dipolar broadening precludes resolution of the hyperfine structure (see Figure S4 in the Supporting Information). In this frame, it is evident that the anisotropy of the ground doublet is of the easy-axis type, with "parallel" transition at low fields, and a non-negligible rhombicity,

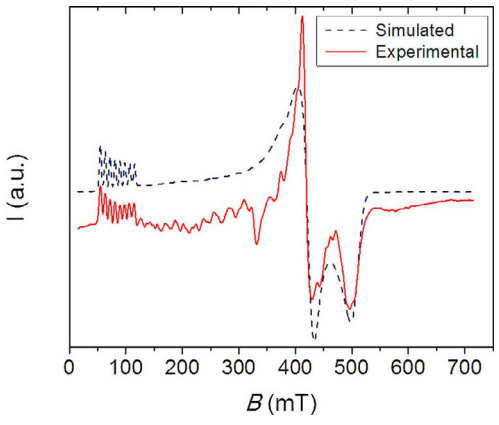

Figure 4. X-band ($\tilde{\nu}=9.43$ GHz) continuous wave EPR spectrum recorded at 5 K on a powder sample of **3** (solid line) and its simulation (dash line).

as evidenced by the separation of the perpendicular transitions in the region 400–500 mT. The experimental spectrum was simulated by using the following spin Hamiltonian [Eq. (4)]:[38]

$$\mathcal{H}' = \mathcal{H}'_{Zeeman} + \mathcal{H}'_{hyperfine} = \mu_B \hat{B} \cdot \bar{g}' \cdot \hat{S}' + \hat{S}' \cdot \bar{A}' \cdot \hat{I}' \qquad (4)$$

in which the primed parameters are associated with the effective spin $S'=1/2$. The best simulation was obtained by assuming an axial hyperfine coupling tensor ($\mathscr{A}'_{1,2}=2\pm1\times10^{-3}$ and $\mathscr{A}'_3=3.20\pm0.05\times10^{-2}$ cm^{-1}) and a moderately rhombic effective $\bar{g}'$ matrix ($g'_1=1.37\pm0.02$, $g'_2=1.62\pm0.02$, and $g'_3=7.930\pm0.002$).

The principal values of the effective $\bar{g}'$ matrix can be related to the spin Hamiltonian parameters of an $S=3/2$ system through the following equations, which are valid only for easy-axis systems (i.e., $D<0$) [Eq. (5)]:[39]

$$g'_1 = g_x\left(1-\frac{1-3\eta}{\sqrt{1+3\eta^2}}\right),\quad g'_2 = g_y\left(1-\frac{1+3\eta}{\sqrt{1+3\eta^2}}\right),\quad g'_3 = g_z\left(\frac{2}{\sqrt{1+3\eta^2}}+1\right) \qquad (5)$$

in which $\eta=E/D$. For purely axial anisotropy ($\eta=0$), Equation (5) affords $g'_1=g'_2=0$ and $g'_3=3g_z$. The non-zero experimental values of g'_1 and g'_2 are then consistent with a significant rhombic anisotropy. It is evident that, depending on the value of η, different solutions for g_x, g_y, and g_z can be found because the problem is over-parametrized. However, sets of solutions in reasonable accordance with those extrapolated from magnetic measurements and confirmed by CTM measurements can be found by assuming the rhombicity to lie in the range $-0.28<\eta<-0.22$. In particular, if one fixes $\eta=-0.273$, as obtained from the magnetic analysis, the application of Equation (5) provides the following estimates of the principal *g* values for the $S=3/2$ system: $g_x=2.125$, $g_y=1.935$, and $g_z=2.825$ (alternatively, assuming $\eta=0.273$, $g_x=1.935$, $g_y=2.125$, and $g_z=2.825$). We note that no reproduction of the effective g' pattern can be obtained for $\eta=0.273$ and $g_x>g_y$ or for $\eta=-0.273$ and $g_y>g_x$. The outcome of this analysis is that the $\bar{g}$ matrix also has a non-negligible rhombicity, which can be clearly detected only by EPR analysis, whereas the magnetic characterization techniques are mainly sensitive to $\bar{D}$ anisotropy. It should also be noted that the only way to reconcile the Hamiltonian description in Equation (4) with that of the Hamiltonian description in Equation (1) is by assuming that the $\bar{g}$ and $\bar{D}$ matrices for the $S=3/2$ state have opposite rhombicities. This means that the smallest $\bar{g}$ principal value is collinear with the intermediate direction of the $\bar{D}$ tensor, whereas the intermediate $\bar{g}$ component is along the hard direction of the $\bar{D}$ tensor. The resulting partial compensation of the two rhombicities is consistent with the relatively small separation of the perpendicular transitions at high field. At first sight, such behavior is counterintuitive because both anisotropies arise from the same phenomenon, that is, spin-orbit coupling (SOC).

Finally, we measured the angular dependence of the X-band EPR spectrum of a single crystal of **1** at low temperature to assign the easy, hard, and intermediate directions of the mag-

netic anisotropy of the ground doublet. The sample was set to rotate around the *b* axis from $\theta = 0^\circ$, where **B** is parallel to the *c* axis, to $\theta = 90^\circ$, where **B** is parallel to the $-a^*$ axis, as in Rot1 of the CTM measurements. The angular dependence of the spectra is shown in Figure 5. The maximum resonant field ($B_{res} = 491.5$ mT, thus corresponding to $g_{eff} = 1.37$) is observed at $\theta = 40^\circ$, whereas the minimum is found at $\theta = 130^\circ$ ($B_{res} = 85.7$ mT, $g_{eff} = 7.93$). Within experimental error ($\pm 5^\circ$), these two extremes occur along the principal directions of the $\bar{D}$ tensor, as determined by CTM (Figure 3). Furthermore, because $g_{eff} = 1.37$ and 7.93 are also the highest and lowest resonance fields observed in the powder spectrum (Figure 4), both the easy and hard directions of g_{eff} lie in the a^*c plane, thus confirming our assignment of *b* as the intermediate anisotropy axis, although it corresponds to the smallest component of the true $\bar{g}$ tensor.

An alternative description of the electronic structure of distorted octahedral cobalt(II), which explicitly takes into account the unquenched orbital angular momentum, should involve the use of the Griffith Hamiltonian [Eq. (6)]:[40]

$$\mathcal{H} = -\frac{3}{2}\kappa\lambda\hat{L}\cdot\hat{S} + \Delta_{ax}\left[\hat{L}_z^2 - \frac{1}{3}L(L+1)\right] + \Delta_{rh}\left[\hat{L}_x^2 - \hat{L}_y^2\right] + \mu_B\mathbf{B}\cdot\left(g_e\hat{S} - \frac{3}{2}\kappa\hat{L}\right) \quad (6)$$

which operates on the ground $^4T_{1g}$ term of the octahedral cobalt(II) ion. By using the T–P isomorphism,[41] the orbital ($L = 1$) and spin ($S = 3/2$) angular momenta interact through SOC, as described by the first term of the Hamiltonian. Here, the orbital-reduction parameter (κ) takes into account the covalence effect and the mixing of $^4T_{1g}(^4F)$ with $^4T_{1g}(^4P)$ due to the crystal field, whereas $-3/2$ is a constant required by T–P isomorphism. The second term of this Hamiltonian represents the effect of an axial crystal field, thus resulting in a splitting of the orbital triplet $^4T_{1g}$ in octahedral symmetry into $^4A_{2g}$ ($M_L = 0$) and ^4E_g ($M_L = \pm 1$) in tetragonal symmetry. The third term models the rhombic component of the crystal field, which removes the degeneracy of the orbital doublet as symmetry is further lowered to C_2. In this framework, a negative (positive) value of Δ_{ax} results in a ground $^4E_g(^4A_{2g})$ term and corresponds to easy-axis (easy-plane) anisotropy.[34,42,43] Finally, the fourth term is the Zeeman interaction, which comprises spin and orbital contributions. Despite the large number of parameters, by fixing the SOC constant to the free-ion value ($\lambda = -180$ cm^{-1}), the pattern of effective *g* factors for the ground doublet could be reproduced[38] by using parameters that lie in a relatively narrow range, that is, $-2100 < \Delta_{ax} < -1650$, $100 < \Delta_{rh} < 160$ cm^{-1}, $0.8 < \kappa < 1.0$ (see Figure S5 in the Supporting Information). The best agreement was found for $\Delta_{ax} = -1850$, $\Delta_{rh} = 130$, $\kappa = 0.9$, $\lambda = -180$ cm^{-1}, which correspond to $|\Delta_{rh}/\Delta_{ax}| \approx 0.07$. With this set of parameters, the first- and second-excited spin-orbit doublets lie at 210 and 558 cm^{-1} from the ground state, respectively (see Table S6 in the Supporting Information). This outcome suggests that a spin Hamiltonian formalism might not be entirely appropriate for modeling the high-temperature magnetic behaviour because the thermal energy is not completely negligible compared to the second-excited doublet. Interestingly, when the same set of parameters is used to simulate the powder dc magnetic data, the resulting curves are in reasonable agreement with the experimental ones (see Figure S6 in the Supporting Information). On the other hand, if applied to torque measurements, the same set of values reproduces the experimental data of Rot1 well, but is less accurate in simulating the data of Rot2 at 100 K (see Figure S7 in the Supporting Information). This outcome indicates that even this approach is too approximate to capture the finest details of the electronic structure of this system and in particular the information related to rhombicity.

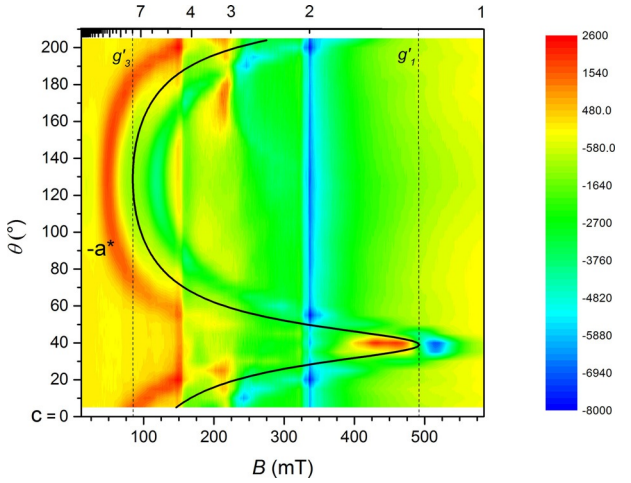

Figure 5. Angular dependence of the resonant fields of the X-band ($\tilde{\nu} = 9.41$ GHz) EPR of a single crystal of **1** at 5 K. The black solid line is the simulated angular dependence of the resonance field by using the parameters reported in the text. The blue line marks a $g = 2.00$ reference impurity in the cavity.

Dynamic magnetic properties

Ac magnetic susceptibility measurements of **1** in zero static field did not display any temperature-dependent peak in out-of-phase susceptibility (χ_M'') measurements. The Kramers nature of the cobalt(II) ion suggests that quantum-tunneling (QT) relaxation paths, induced by hyperfine interactions or intermolecular dipolar couplings, accelerate the relaxation of the magnetization beyond detection. In a static field of 1 kOe, however, clear maxima appeared in the frequency range 10–10000 Hz, the position of which are temperature dependent (see Figure 6a and Figure S8 in the Supporting Information). Treatment of the isothermal $\chi_M''(\nu)$ plots with a generalized Debye model allowed us to extract the relaxation time (τ) at each temperature.[44] These data are shown in Figure 6b as a plot of $\ln\tau(1/T)$. At the highest-temperature interval between 6.5 and 9.5 K, the plot appears to be linear and can be suitably fitted with the Arrhenius law ($\ln\tau = \ln\tau_0 + U_{eff}/k_BT$) with the best-fit parameters $U_{eff}/k_B = 43.6(2)$ K and $\tau_0 = 1.2(2)\times10^{-7}$ s (green line in Figure 6b). These values are in the range previously observed for field-induced pseudo-octahedral mononuclear SMMs.[45] The observed activation barrier to magnetic re-

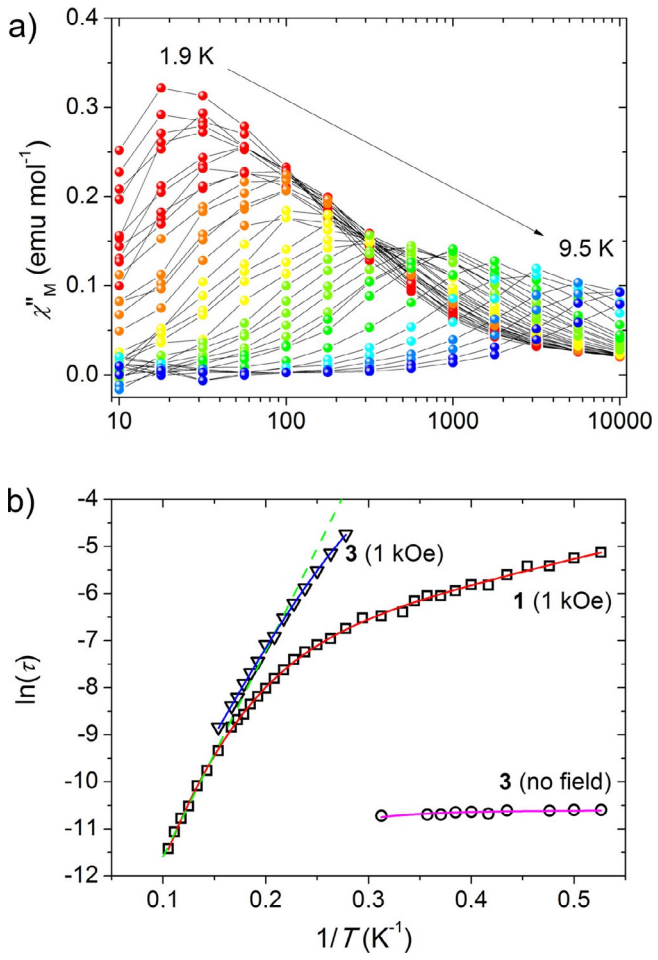

Figure 6. a) Imaginary component of the ac susceptibility (χ_M'') of **1** measured at an applied static field of 1 kOe in the frequency range 10–10 000 Hz and in the temperature range 1.9 (red)–9.5 (blue) K (the gray lines are given as a guide for the eye). b) Arrhenius plot for **1** at an applied static field of 1 kOe (□) and for **3** in a zero field (▽) and a static field of 1 kOe (○). The green dotted line is given by the fitting of **1** in the range 6.5–9.5 K with an Orbach model, whereas the red curve employs a mixed Raman and direct model. The magenta and blue lines display the data fitting of **3** at zero field and an applied field of 1 kOe, respectively (see the text for further discussion).

laxation, however, is well below the splitting between the two lowest-lying doublets (127 cm^{-1} or 165 K, as estimated from dc magnetic data of **1**; see above). On lowering the temperature, a distinct curvature appears in the plot. This deviation from the simple Arrhenius-like behavior can be due to processes induced by either nonresonant spin-phonon interactions in the solid state[46,47] or tunnel mechanisms. To reproduce the temperature dependence of the magnetic relaxation over the whole temperature range, QT (A), direct (BT), and Raman (CT^n) relaxation processes were taken into account in addition to the previous Orbach term, as outlined by Equation (7):

$$\tau^{-1} = \tau_0{}^{-1} \exp(-U_{eff}/k_B T) + A + BT + CT^n \quad (7)$$

To avoid over-parametrization, the number of fitting terms was kept as low as possible and the quantum-tunneling mechanism was considered to be quenched by the applied static field ($A = 0$). Upon either including an Orbach mechanism (with fixed τ_0 and U_{eff} values taken from the high-temperature region) or excluding the Raman term, the model was unable to account for the low-temperature relaxation behavior. A Raman process along with direct phonon-induced relaxation at low temperature ($C = 0.45(8)$ s^{-1}K^{-n}, $n = 5.38(9)$, $B = 103(4)$ K^{-1}) gave the best results (red line in Figure 6b). The exponent n of the Raman relaxation process for a Kramer ion should be equal to 9,[20,48] but several factors can contribute to lower its value,[20] such as the presence of low-lying excited electronic states, for which $n = 5$ is postulated.[48]

Dipolar interactions in the solid state can provide efficient relaxation pathways in zero field and hinder the detection of magnetization dynamics. Dilution of SMMs in a diamagnetic matrix has been identified as a key tool for reducing such long-range couplings, thus affording a measurable zero-field relaxation.[14,49] The effect of dipolar interactions in **1** was then ascertained by analysing the ac response of diamagnetically diluted sample **3**. Unlike in **1**, a set of clearly visible peaks appeared in the $\chi_M''(\nu)$ isothermal profiles of **3** in zero field in the range 1.9–3.2 K (see Figure S9 in the Supporting Information). The maxima of these peaks display a feeble dependence on temperature that could be reproduced considering a Raman relaxation process with QT. A best-fit procedure, the results of which are reported as a magenta line in Figure 6b, yielded $C = 11(2)$ s^{-1}K^{-n} and a tunneling frequency of $A = 40.3(5)$ kHz, with the n exponent fixed at 5.38 as in **1** to avoid over-parametrization. The onset of a QT relaxation path in zero field is in line with the rhombicity of **1** and the unavoidable presence of hyperfine interactions, which are necessary to promote tunneling. These data show for the first time, to the best of our knowledge, that slow magnetic relaxation in zero field can be achieved in a pseudo-octahedral cobalt(II) complex, provided that intermolecular magnetic interactions are efficiently reduced. A similar effect given by magnetic dilution on easy-axis systems was previously reported only in a tetrahedral cobalt(II) compound.[14] It is also most probably the reason for zero-field slow magnetic relaxation in the $Co^{II}Co^{III}_3$ SMM family, in which the magnetically active trigonal prismatic cobalt(II) ion is partly isolated from the neighbouring paramagnetic centers by three diamagnetic cobalt(III) ions.[18]

Upon application of a static field of 1 kOe, the magnetization dynamics of **3** slows down significantly due to the further suppression of relaxation pathways induced by QT (see Figure S10 in the Supporting Information). The high-temperature data almost overlap with the data detected for **1**, thus suggesting that when a linear regime in the Arrhenius plot is observed the effective barrier is much smaller than the separation between the ground and the first-excited doublets. This finding indicates the key role played by nonresonant phonons in the high-temperature range.[46] The data can be phenomenologically reproduced including Raman and direct relaxation processes (blue line in Figure 6b), as for data fitting of **1**. The best-fit parameters ($C = 0.015(5)$ s^{-1}K^{-n}, $n = 7.0(2)$, $B = 0(4)$ K^{-1}) indicate that application of a dc field of 1 kOe suppresses the direct pathway and leads to an increased n exponent, in line

Table 2. *D* values, *E* values, diagonalized $\tilde{g}$ and $\tilde{D}$ matrices, and energy differences between the ground and the first-excited KD (Δ_E).[a]

Method	g_{xx}, g_{yy}, g_{zz}	D_{xx}, D_{yy}, D_{zz} [cm^{-1}]	D [cm^{-1}]	E [cm^{-1}]	Δ_E [cm^{-1}]	δ_E [cm^{-1}]
ORCA/CASSCF	2.156, 1.945, 3.069	48.68, 13.42, −62.11	−93.2	17.6	196.1	364.7
ORCA/NEVPT2	2.152, 1.960, 3.004	43.11, 14.34, −57.45	−86.2	14.4	179.4	467.4
MOLCAS/CASSCF	2.169, 1.963, 3.070	49.22, 12.19, −61.41	−92.1	18.5	195.1	368.9
MOLCAS/CASPT2	2.149, 1.960, 3,058	47.30, 13.25, −60.55	−90.8	17.0	191.0	364.6

[a] Computed by using the structure of **1** at 161 K with different methods and the standard basis set (see the Supporting Information); for comparison, the first-excitation energy (δ_E) in the absence of SOC for the ground state is also reported.

with a previous report on trigonal antiprismatic cobalt(II) complexes with uniaxial anisotropy.[50]

Theoretical calculations

To better understand and quantify the overall electronic structure of the cobalt(II) center and its magnetic anisotropy in **1**, ab initio multireference calculations that used the ORCA[51] and MOLCAS[52] software packages were carried out. The ORCA software produces two sets of results: CASSCF and NEVPT2, both including spin-orbit contributions introduced by the quasidegenerate perturbation theory (QDPT). The MOLCAS software was employed to provide CASSCF and CASPT2 results, including spin-orbit effects that have been introduced with the SO-RASSI method. Tables S7–S10 (see the Supporting Information) report the spin-free (δ_E) and spin-orbit (Δ_E) state energies, and Table 2 and Tables S11 and S12 (see the Supporting Information) gather the second-order anisotropy parameters, as described by Eq. (1), the diagonalized $\tilde{g}$ and $\tilde{D}$ matrices and the energy differences between the ground and the first-excited Kramers doublet (KD) computed with different methods and the standard basis set, starting from the structure of **1** at 161 and 295 K.

Before including the spin-orbit effects, all the calculations agree indicating an orbitally nondegenerate $S=3/2$ ground state. In fact, the crystal-field term of the octahedrally coordinated high-spin cobalt(II) ion ($^4T_{1g}$) splits into three orbital singlets as the symmetry is lowered to C_2. Each of these orbitally nondegenerate spin quartets is further split by SOC into two KDs (see Figure S11 in the Supporting Information). In all the calculations, the ground and first-excited KDs are energetically well separated from the higher KDs, thus suggesting that a spin Hamiltonian formalism may be justified in the present case. Moreover, the energy of the first-, second-, and third-excited doublets (ca. 191, 648, and 929 cm^{-1}, respectively, determined by using MOLCAS/CASPT2) resemble the energies found when the Griffith Hamiltonian is employed to reproduce the EPR data (i.e., 210, 558, and 820 cm^{-1}, respectively; see Table S6 in the Supporting Information).

These calculations also produce similar and negative values of *D*, with a negligible effect due to the use of the molecular structures at the two different temperatures (i.e., 161 and 295 K; see Table S11 in the Supporting Information). However, a small but systematic trend can be observed, which consists of a decrease in the $|D|$ value and an increase in the value of *E* upon cooling. The calculated $|D|$ values are approximately 50% larger than when obtained from the fitting of the experimental magnetic data, whereas the computed values of *E* are in good agreement with the experiments. To evaluate the possible effect of the employed basis set on the computed *zfs* parameters, the calculations were repeated with a larger basis set for the structure of **1** at 161 K (see the Experimental Section and Table S12 in the Supporting Information). The new results show just small differences relative to the standard basis, with slightly larger $|D|$ and *E* values. The effect is more pronounced in MOLCAS than in ORCA.

The sign and value of *D* can be rationalized by using the spin-orbit operator, which is responsible for the coupling between the ground and excited states.[10,53] When the excitation occurs between orbitals with the same $|m_l|$ values, the $M_S=\pm 3/2$ components become more stable, and thus a negative contribution to the *D* value is obtained. On the other hand, an excitation between orbitals that involves a $|\Delta m_l|=1$ change, which produces stabilized $M_S=\pm 1/2$ components, leads to a positive contribution to the *D* value. Compound **1** displays a distorted octahedral core that produces the d-orbital splitting shown in Figure 7, which is obtained from the ORCA/NEVPT2

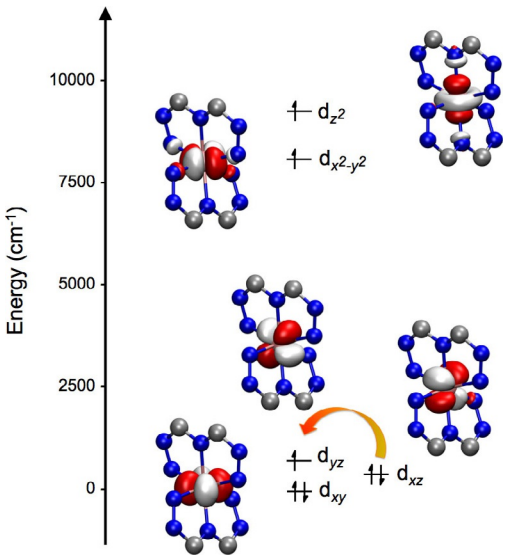

Figure 7. AILF-computed d-orbital splitting for **1** (orbital energies: $d_{xy}=0.0$, $d_{xz}=444.6$, $d_{yz}=697.9$, $d_{x2-y2}=8121.0$, $d_{z2}=9257.3$ cm^{-1}). Co = pink, C = gray, N = blue; hydrogen atoms and part of the ligands have been omitted for clarity. The orange arrow indicates the lowest-energy transition.

calculation by using the ab initio ligand-field theory (AILF).[10,54] As may be observed, the degeneracy of the t_{2g} and e_g orbitals of the regular octahedron is lifted, which indicates that the initial octahedral $^4T_{1g}$ ground state should evolve into a lower-energy term in C_2 symmetry (see Figure S11 in the Supporting Information). The AILF method allows the identification of the d orbitals in **1** after splitting, and the lowest-energy doubly occupied orbital is d_{xy}, which is followed by the doubly occupied orbital d_{xz} (or d_{yz} because these orbitals cannot be distinguished), whereas the first semioccupied orbital is d_{yz} (or d_{xz}; where *z* represents the *trans*-N{pyridyl}-Co-N{pyridyl} direction and *x* and *y* represent the directions of the pyrazolyl nitrogen atoms). The other two orbitals (d_{x2-y2} and d_{z2}) are found at higher energies. Thus, the first excitation should occur within the d_{xz}/d_{yz} orbital pair and, because these orbitals have the same $|m_l|$ value, the larger contribution to the *D* value should be negative; consequently, the magnetic easy-axis nature of **1** is confirmed. This outcome is in opposition with the most common orbital splitting for pseudo-octahedral cobalt(II) complexes, which usually yields the d_{xy} orbital as the first semioccupied orbital,[31] and subsequently resulting in easy-plane systems.

The calculated $\tilde{\boldsymbol{D}}$ matrix has its intermediate axis (i.e., *y* in Eq. (1) with $E>0$) along the twofold crystallographic *b* axis and the hard (*x*) and easy (*z*) directions in the *a***c* plane (see Figure S12 in the Supporting Information), with the hard *x* axis at 10° from *a*. Thus, the computed orientation of the *zfs* tensor compares very well with that obtained by single-crystal CTM measurements and EPR spectroscopic analysis. Turning now to *g* factors, the ab initio values (Table 2) are remarkably close to the values obtained by using Equation (5). For example, the *g* factors that result from ORCA/NEVPT2 calculations are $g_x=2.152$, $g_y=1.960$, and $g_z=3.004$, which can be compared with the *g* factors estimated by analysis of the EPR spectra, that is, $g_x=2.125$, $g_y=1.935$, and $g_z=2.825$. The effective $\tilde{\boldsymbol{g}}'$ factors of the ground KD found in this same calculation, which can be directly compared with the values obtained from the EPR experiments, are slightly more anisotropic, that is, $g'_1=0.999$, $g'_2=1.172$, and $g'_3=8.566$ (from EPR: $g'_1=1.37\pm0.02$, $g'_2=1.62\pm0.02$, and $g'_3=7.930\pm0.002$). The results obtained in the MOLCAS/CASPT2 calculation are also quite similar to both these sets of values, that is, $g'_1=1.108$, $g'_2=1.287$, and $g'_3=8.570$. The principal directions of the $\tilde{\boldsymbol{g}}$ matrix are collinear with those of $\tilde{\boldsymbol{D}}$, in which the largest *g* factor is along the *z* direction. However, the smallest *g* value is computed along the twofold crystallographic axis (*y*) rather than along the hard direction of $\tilde{\boldsymbol{D}}$ (*x*) (see Figure S12 in the Supporting Information). As observed in the single-crystal EPR experiments, the theoretical calculations indicate an inversion of the intermediate and hard axes between $\tilde{\boldsymbol{g}}$ and $\tilde{\boldsymbol{D}}$, that is, opposite rhombicities.

The CTM experiments can be nicely reproduced in the MOLCAS calculations by recomputing the magnetization of the system along the different axes upon application of a rotating magnetic field (see the Experimental Section in the Supporting Information for further details). The agreement between the experimental and theoretical torque values for Rot1 in the temperature range 10–100 K is very satisfactory, whereas some discrepancy is observed in Rot2 when increasing the temperature (see Figures S13 and S14 in the Supporting Information), as observed by applying the Griffith model. It is important to underline that Rot2, which mainly probes the intermediate and hard magnetic directions, is mostly affected by the inversion of the corresponding components of the $\tilde{\boldsymbol{g}}$ and $\tilde{\boldsymbol{D}}$ matrices; the origin of this phenomenon remains unclear.

The spin-relaxation pathways, which can be related to the dynamic magnetic properties of transition-metal complexes, can be obtained directly through the SINGLE ANISO[55] code implemented in the MOLCAS software. The computed relative energies of the lowest-lying KDs and the magnetization reversal pathway for **1**, as obtained by applying the MOLCAS/CASPT2 calculation, are shown in Figure 8. The calculations indicate a plausible relaxation pathway through a direct QT in the ground state; the matrix element of the transition within the 1−/1+ ground doublet takes a value of 0.40, which is higher than the required threshold of 0.1 for an efficient relaxation mechanism.[10] In addition, an Orbach process could be also plausible; for example, the first-excited KD is quite low in energy (191.0 cm^{-1}) and the matrix elements related to the vertical and diagonal (Orbach) excitations are high enough (1.09 and 1.11, respectively) to allow the spin relaxation through these pathways. However, the experimental effective barrier for the thermally activated process is significantly smaller than the calculated barrier. Obviously, the horizontal transition between the 2− and 2+ states is allowed, thus enabling the possibility of QT between them. The second- and third-excited KDs are much higher in energy and, therefore, are not expected to participate in the relaxation mechanism. These results, combined with the ac magnetic susceptibility measurements of **1**, confirm the spin-phonon Raman relaxation mechanism.

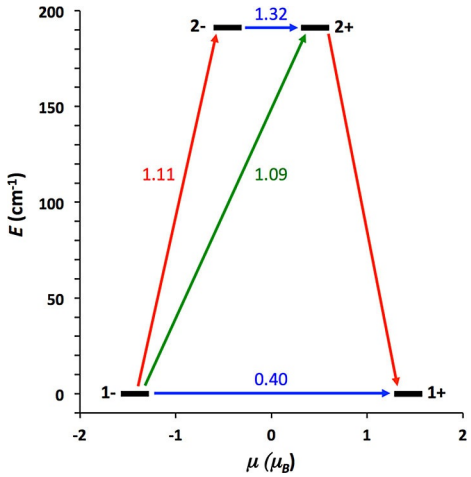

Figure 8. Lowest two KDs and the ab initio MOLCAS/CASPT2 computed relaxation mechanism for **1**. The thick black lines imply KDs as a function of their magnetic moment along the main anisotropy axis. Red lines indicate the magnetization reversal mechanism. Blue lines correspond to ground state QT and thermally assisted QT through the first-excited KD. Green lines show the possible Orbach relaxation processes. The values close to the arrows indicate the matrix elements of the transition magnetic moments (i.e., an efficient spin relaxation mechanism is expected if the matrix elements are greater than 0.1).

If **1** were to follow the Orbach mechanism depicted by the calculations, the U_{eff} value would take a higher value than the value obtained in the fitting (i.e., 43.6(2) K), which is clearly not the case, thus indicating that the spin-relaxation pathway does not proceed by overcoming a thermal activation barrier. This behavior is quite general for systems with large D values, and an explanation can be based on the fact that the Arrhenius law is only expected if the Debye description of the phonons is correct. A much smaller energy barrier and a deviation from the Arrhenius law at low temperature can be ascribed to the anharmonicity of the vibrational modes (a source of Raman-like relaxation).

Conclusion

We have presented detailed magnetic and spectroscopic characterizations, both on powder and single-crystal samples, of a pseudo-octahedral cobalt(II) complex, which we have used as a test bench for different theoretical approaches that ranged from ab initio calculations to the ligand-field model and spin Hamiltonian descriptions. We can conclude that the main features of the magnetic behavior of this system are accounted for by using an $S=3/2$ spin Hamiltonian approach. However, by exploiting the variety of the experimental and theoretical techniques employed, we were also able to evidence the hitherto unreported inversion of the hard and intermediate axes of $\tilde{\boldsymbol{g}}$ and $\tilde{\boldsymbol{D}}$ matrices, a phenomenon that was nicely reproduced by ab initio calculations.

The present results have further highlighted the possibility of obtaining slow magnetic relaxation in a mononuclear pseudo-octahedral HS cobalt(II) complex with dominant easy-axis anisotropy in the absence of an applied dc field. In particular, the distortion of the coordination environment from a perfect octahedral geometry, as created by the two *mer* bpp-COOMe ligands in **1**, induces the easy-axis nature of the compound.

The observed magnetization dynamics is strongly affected by tunnel processes due to the rhombic magnetic anisotropy in zero field. In an applied magnetic field, the behavior deviated from the Arrhenius behavior expected for an ideal SMM as the highest estimation of the energy barrier to be overcome is significantly smaller than the separation between the ground and first doublets. This behavior has been observed in other highly anisotropic complexes[56] and attributed to the efficiency of nonresonant optical phonons,[46,47] which cannot be neglected if anharmonicity is taken into account. Even if the optimization of the magnetization dynamics of SMM requires the control of several factors, such as tunneling mechanisms and vibrational modes, the rational design of the coordination environment remains the first step to be able to generate magnetic bistability through the appropriate sign of the magnetic anisotropy. An octahedral cobalt(II) environment, despite its large orbital contribution, has so far eluded the successful provision of examples of genuine SMM behavior. The combination of a detailed experimental investigation with theoretical modeling at different levels, as described herein, can provide valuable hints for a rational design of cobalt(II)-based SMMs.

Experimental Section

General information

$Co(ClO_4)_2{\cdot}6H_2O$ and $Zn(ClO_4)_2{\cdot}6H_2O$ were of reagent grade and used as received. Diethyl ether was predried over $CaCl_2$ overnight and distilled from sodium/benzophenone under N_2 before use. CH_3CN was treated with CaH_2 and distilled under N_2. Elemental analyses were recorded on a Carlo Erba EA1110 CHNS-O automatic analyser. The Zn and Co content in **3** were evaluated with a PerkinElmer Optima 5300 DV inductively coupled plasma optical emission spectrometer equipped with a concentric nebulizer. ^{1}H NMR spectra were recorded on a 400 MHz Bruker FT-NMR Advance400 spectrometer at room temperature. Proton chemical shifts are given in parts per million (ppm) versus external TMS and were determined by reference to the solvent residual signals ($\delta=1.94$ ppm for CHD_2CN); coupling constants are given in Hz. IR spectra were recorded as KBr discs on a Jasco FTIR-4700LE spectrophotometer with a resolution of 2 cm^{-1}. The bpp-COOMe ligand was synthesized as previously reported.[26] Further details on the X-ray structure determination of **1** and **2** (see Table S1 in the Supporting Information), dc and ac magnetic measurements, CTM and EPR experiments, and the theoretical calculations can be found in the Supporting Information.

Synthesis of bis[methyl 2,6-di(pyrazol-1-yl)pyridine-4-carboxylate]cobalt(II) bis(perchlorate) $[Co(bpp\text{-}COOCH_3)_2](ClO_4)_2$ (1)

Ligand bpp-COOMe (36.0 mg, 0.134 mmol) was suspended in acetonitrile (3 mL). The addition of $Co(ClO_4)_2{\cdot}6H_2O$ (24.3 mg, 0.0664 mmol) to the reaction mixture caused dissolution of the ligand upon formation of the desired complex with an immediate color change to purple/red. After stirring for 30 min, the filtered solution was subjected to vapour diffusion with diethyl ether (5 mL). X-ray-quality light-red crystals appeared within 1 day and were collected after 1 week at complete diffusion (39.4 mg, 74.5 %). IR (KBr): $\tilde{\nu}_{max}=1738$ (s; νC=O ester), 1632 (s), 1580 (s), 1523 (s) and 1405 (s) (νC=N and νC=C), 1460 (s) and 1444 (m) (δC–H), 1095 (s; νClO_4^-), 1056 (s; νC–O) cm^{-1}; elemental analysis (%) calcd for $C_{26}H_{22}Cl_2CoN_{10}O_{12}$ (796.35): C 39.21, H 2.78, N 17.59; found: C 39.90, H 2.88, N 17.99.

Synthesis of bis[methyl 2,6-di(pyrazol-1-yl)pyridine-4-carboxylate]zinc(II) bis(perchlorate) $[Zn(bpp\text{-}COOCH_3)_2](ClO_4)_2$ (2)

The above-described procedure was employed using bpp-COOMe (39.0 mg, 0.145 mmol) and $Zn(ClO_4)_2{\cdot}6H_2O$ (27.6 mg, 0.0741 mmol) to afford colorless crystals suitable for X-ray diffraction studies (40.0 mg, 68.8 %).^{1}H NMR (400 MHz, CD_3CN, 293 K): $\delta=8.73$ (d, $J_1=2.8$ Hz, 2H; H^5-pz), 8.45 (s, 2H; $H^{3/5}$-py), 7.62 (d, $J_2=1.6$ Hz, 2H; H^3-pz), 6.70 (dd, $J_1=2.8$, $J_2=1.6$ Hz, 2H; H^4-pz), 4.11 ppm (s, 3H; OCH_3); IR (KBr): $\tilde{\nu}_{max}=1738$ (s; νC=O ester), 1632 (s), 1584 (s), 1522 (s) and 1405 (s) (νC=N and νC=C), 1458 (s) and 1444 (m) (δC–H), 1095 (s; νClO_4^-), 1058 (s; νC–O) cm^{-1}; elemental analysis (%) calcd for $C_{26}H_{22}Cl_2N_{10}O_{12}Zn$ (802.83): C 38.90, H 2.76, N 17.45; found: C 39.05, H 3.04, N 17.48.

Synthesis of $[Zn_{0.95}Co_{0.05}(bpp\text{-}COOCH_3)_2](ClO_4)_2$ (3)

The above-described procedure was employed using bpp-COOMe (81.2 mg, 0.302 mmol), $Co(ClO_4)_2{\cdot}6H_2O$ (2.9 mg, 0.0079 mmol), and $Zn(ClO_4)_2{\cdot}6H_2O$ (53.9 mg, 0.145 mmol) in acetonitrile (6 mL) and di-

ethyl ether (10 mL) to afford very light-orange crystals suitable for X-ray diffraction studies (91.7 mg, 75.8%). IR (KBr): $\tilde{\nu}_{max} = 1737$ (s; νC=O ester), 1632 (s), 1584 (s), 1522 (s) and 1405 (s) (νC=N and νC=C), 1458 (s) and 1444 (m) (δC–H), 1095 (s; νClO_4^-), 1058 (s; νC–O) cm^{-1}; elemental analysis (%) calcd for $C_{26}H_{22}Cl_2N_{10}O_{12}Zn_{0.95}Co_{0.05}$ (802.51): C 38.91, H 2.76, N 17.45, Co 0.37, Zn 7.74; found: C 39.22, H 2.83, N 17.46, Co 0.40, Zn 8.04.

Acknowledgements

We thank the European Research Council, the Italian Ministero dell'Istruzione, dell'Università e della Ricerca (MIUR), the Polish Ministry of Science and Higher Education, and the Spanish Ministerio de Economía *y* Competitividad for funding through Advanced Grant MolNanoMas no. 267746, FIRB project no. RBAP117RWN, the Iuventus Plus Programme grant agreement no. 0370/IP3/2015/73, and grant CTQ2015-64579-C3-1-P, MINECO/FEDER, UE, respectively. All authors kindly acknowledge COST CA 15128. E.R. thanks the Generalitat de Catalunya for an ICREA Academia award. J.J. and E.R. thankfully acknowledge the computer resources in the Consorci Serveis Universitaris de Catalunya (CSUC). L.S. and L.T. acknowledge the help of Dr. Mauro Perfetti (University of Copenhagen) for helping in preliminary CTM measurements and data analysis.

Conflict of interest

The authors declare no conflict of interest.

Keywords: ab initio calculations · cobalt · EPR spectroscopy · single-molecule magnets · torque magnetometry

[1] D. Gatteschi, R. Sessoli, J. Villain, *Molecular Nanomagnets*, Oxford University Press, Oxford, **2006**.

[2] J. D. Rinehart, M. Fang, W. J. Evans, J. R. Long, *J. Am. Chem. Soc.* **2011**, *133*, 14236 – 14239.

[3] a) F.-S. Guo, B. M. Day, Y.-C. Chen, M.-L. Tong, A. Mansikkamaki, R. A. Layfield, *Angew. Chem. Int. Ed.* **2017**, *56*, 11445 – 11449; *Angew. Chem.* **2017**, *129*, 11603 – 11607; b) C. A. P. Goodwin, F. Ortu, D. Reta, N. F. Chilton, D. P. Mills, *Nat. Lett.* **2017**, *548*, 439 – 442.

[4] a) M. Mannini, F. Pineider, C. Danieli, F. Totti, L. Sorace, Ph. Sainctavit, M.-A. Arrio, E. Otero, L. Joly, J. C. Cezar, A. Cornia, R. Sessoli, *Nature* **2010**, *468*, 417 – 421; b) C. Wäckerlin, F. Donati, A. Singha, R. Baltic, S. Rusponi, K. Diller, F. Patthey, M. Pivetta, Y. Lan, S. Klyatskaya, M. Ruben, H. Brune, J. Dreiser, *Adv. Mater.* **2016**, *28*, 5195 – 5199.

[5] a) L. Rigamonti, M. Piccioli, L. Malavolti, L. Poggini, M. Mannini, F. Totti, B. Cortigiani, A. Magnani, R. Sessoli, A. Cornia, *Inorg. Chem.* **2013**, *52*, 5897 – 5905; b) L. Rigamonti, M. Piccioli, A. Nava, L. Malavolti, B. Cortigiani, R. Sessoli, A. Cornia, *Polyhedron* **2017**, *128*, 9 – 17.

[6] a) O. Sato, *Nat. Chem.* **2016**, *8*, 644 – 656; b) D. Pinkowicz, M. Rams, M. Mišek, K. V. Kamenev, H. Tomkowiak, A. Katrusiak, B. Sieklucka, *J. Am. Chem. Soc.* **2015**, *137*, 8795 – 8801.

[7] a) P. Parois, S. A. Moggach, J. Sanchez-Benitez, K. V. Kamenev, A. R. Lennie, J. E. Warren, E. K. Brechin, S. Parsons, M. Murrie, *Chem. Commun.* **2010**, *46*, 1881 – 1883; b) S. A. Corrales, J. M. Cain, K. A. Uhlig, A. M. Mowson, C. Papatriantafyllopoulou, M. K. Peprah, A. Ozarowski, A. J. Tasiopoulos, G. Christou, M. W. Meisel, C. Lamprapoulos, *Inorg. Chem.* **2016**, *55*, 1367 – 1369.

[8] a) A. Prescimone, C. J. Milios, J. Sanchez-Benitez, K. V. Kamenev, C. Loose, J. Kortus, S. A. Moggach, M. Murrie, J. E. Warren, A. R. Lennie, S. Parsons, E. K. Brechin, *Dalton Trans.* **2009**, 4858 – 4867; b) A. Prescimone, J. Sanchez-Benitez, K. V. Kamenev, S. A. Moggach, A. R. Lennie, J. E. Warren, M. Murrie, S. Parsons, E. K. Brechin, *Dalton Trans.* **2009**, 7390 – 7395; c) C. H. Woodall, G. A. Craig, A. Prescimone, M. Misek, J. Cano, J. Faus, M. R. Probert, S. Parsons, S. Moggach, J. Martinez-Lillo, M. Murrie, K. V. Kamenev, E. K. Brechin, *Nat. Commun.* **2016**, *7*, 13870; d) G. A. Craig, A. Sarkar, C. H. Woodall, M. A. Hay, K. E. R. Marriott, K. V. Kamenev, S. A. Moggach, E. K. Brechin, S. Parsons, G. Rajaraman, M. Murrie, *Chem. Sci.* **2018**, *9*, 1551 – 1559.

[9] F. D. Natterer, K. Yang, W. Paul, P. Willke, T. Choi, T. Greber, A. J. Heinrich, C. P. Lutz, *Nature* **2017**, *543*, 226 – 231.

[10] S. Gómez-Coca, D. Aravena, R. Morales, E. Ruiz, *Coord. Chem. Rev.* **2015**, *289 – 290*, 379 – 392.

[11] a) G. A. Craig, M. Murrie, *Chem. Soc. Rev.* **2015**, *44*, 2135 – 2147; b) J. M. Frost, K. L. M. Harriman, M. Murugesu, *Chem. Sci.* **2016**, *7*, 2470 – 2491.

[12] a) J. M. Zadrozny, D. J. Xiao, M. Atanasov, G. J. Long, F. Grandjean, F. Neese, J. R. Long, *Nat. Chem.* **2013**, *5*, 577 – 581; b) J. M. Zadrozny, D. J. Xiao, J. R. Long, M. Atanasov, F. Neese, F. Grandjean, G. J. Long, *Inorg. Chem.* **2013**, *52*, 13123 – 13131.

[13] S. Mossin, B. L. Tran, D. Adhikari, M. Pink, F. W. Heinemann, J. Sutter, R. K. Szilagyi, K. Meyer, D. J. Mindiola, *J. Am. Chem. Soc.* **2012**, *134*, 13651 – 13661.

[14] a) J. M. Zadrozny, J. R. Long, *J. Am. Chem. Soc.* **2011**, *133*, 20732 – 20734; b) J. M. Zadrozny, J. Telser, J. R. Long, *Polyhedron* **2013**, *64*, 209 – 217.

[15] D.-K. Cao, J.-Q. Feng, M. Ren, Y.-W. Gu, Y. Song, M. D. Ward, *Chem. Commun.* **2013**, *49*, 8863 – 8865.

[16] M. S. Fataftah, J. M. Zadrozny, D. M. Rogers, D. E. Freedman, *Inorg. Chem.* **2014**, *53*, 10716 – 10721.

[17] E. Carl, S. Demeshko, F. Meyer, D. Stalke, *Chem. Eur. J.* **2015**, *21*, 10109 – 10115.

[18] a) Y.-Y. Zhu, C. Cui, Y.-Q. Zhang, J.-H. Jia, X. Guo, C. Gao, K. Qian, S.-D. Jiang, B.-W. Wang, Z.-M. Wang, S. Gao, *Chem. Sci.* **2013**, *4*, 1802 – 1806; b) Y.-Y. Zhu, Y.-Q. Zhang, T.-T. Yin, C. Gao, B.-W. Wang, S. Gao, *Inorg. Chem.* **2015**, *54*, 5475 – 5486.

[19] V. V. Novikov, A. A. Pavlov, Y. V. Nelyubina, M.-E. Boulon, O. A. Varzatskii, Y. Z. Voloshin, R. E. P. Winpenny, *J. Am. Chem. Soc.* **2015**, *137*, 9792 – 9795.

[20] Y. Rechkemmer, F. D. Breitgoff, M. van der Meer, M. Atanasov, M. Hakl, M. Orlita, P. Neugebauer, F. Neese, B. Sarkar, J. van Slageren, *Nat. Commun.* **2016**, *7*, 10467.

[21] X.-N. Yao, J.-Z. Du, Y.-Q. Zhang, X.-B. Leng, M.-W. Yang, S.-D. Jiang, Z.-X. Wang, Z.-W. Ouyang, L. Deng, B.-W. Wang, S. Gao, *J. Am. Chem. Soc.* **2017**, *139*, 373 – 380.

[22] D. Tu, D. Shao, H. Yan, C. Lu, *Chem. Commun.* **2016**, *52*, 14326 – 14329.

[23] A. A. Pavlov, Y. V. Nelyubina, S. V. Kats, L. V. Penkova, N. N. Efimov, A. O. Dmitrienko, A. V. Vologzhanina, A. S. Belov, Y. Z. Voloshin, V. V. Novikov, *J. Phys. Chem. Lett.* **2016**, *7*, 4111 – 4116.

[24] S. Vaidya, S. Tewary, S. K. Singh, S. K. Langley, K. S. Murray, Y. Lan, W. Wernsdorfer, G. Rajaraman, M. Shanmugam, *Inorg. Chem.* **2016**, *55*, 9564 – 9578.

[25] P. E. Kazin, M. A. Zykin, W. Schnelle, Y. V. Zubavichus, K. A. Babeshkin, V. A. Tafeenko, C. Felser, M. Jansen, *Inorg. Chem.* **2017**, *56*, 1232 – 1240.

[26] N. Bridonneau, L. Rigamonti, G. Poneti, D. Pinkowicz, A. Forni, A. Cornia, *Dalton Trans.* **2017**, *46*, 4075 – 4085.

[27] a) M. A. Halcrow, *Coord. Chem. Rev.* **2009**, *253*, 2493 – 2514; b) L. J. Kershaw Cook, R. Mohammed, G. Sherborne, T. D. Roberts, S. Alvarez, M. A. Halcrow, *Coord. Chem. Rev.* **2015**, *289 – 290*, 2 – 12.

[28] M. A. Halcrow, *Chem. Soc. Rev.* **2011**, *40*, 4119 – 4142.

[29] a) Y. Hasegawa, K. Takahashi, S. Kume, H. Nishihara, *Chem. Commun.* **2011**, *47*, 6846 – 6848; b) K. Takahashi, Y. Hasegawa, R. Sakamoto, M. Nishikawa, S. Kume, E. Nishibori, H. Nishihara, *Inorg. Chem.* **2012**, *51*, 5188 – 5198.

[30] L. J. Kershaw Cook, F. L. Thorp-Greenwood, T. P. Comyn, O. Cespedes, G. Chastanet, M. A. Halcrow, *Inorg. Chem.* **2015**, *54*, 6319 – 6330.

[31] S. Gómez-Coca, A. Urtizbarea, E. Cremades, P. J. Alonso, A. Camón, E. Ruiz, F. Luis, *Nat. Commun.* **2014**, *5*, 4300.

[32] Song and co-workers reported the appearance of an out-of-phase ac signal upon diamagnetic dilution of an easy-axis octahedral cobalt(II) derivative, but no maxima were observed in temperature-dependent measurements and no Arrhenius plot was presented; see: J. Li, Y. Han, F. Cao, R.-M. Wei, Y.-Q. Zhang, Y. Song, *Dalton Trans.* **2016**, *45*, 9279 – 9284.

[33] H. A. Jahn, E. Teller, *Proc. R. Soc. London Ser. A* **1937**, *161*, 220 – 235.

[34] E. A. Buvaylo, V. N. Kokozay, O. Yu. Vassilyeva, B. W. Skelton, A. Ozarowski, J. Titiš, B. Vranovičová, R. Boča, *Inorg. Chem.* **2017**, *56*, 6999 – 7009.
[35] N. F. Chilton, R. P. Anderson, L. D. Turner, A. Soncini, K. S. Murray, *J. Comput. Chem.* **2013**, *34*, 1164 – 1175.
[36] L. Rigamonti, A. Cornia, A. Nava, M. Perfetti, M.-E. Boulon, A.-L. Barra, X. Zhong, K. Park, R. Sessoli, *Phys. Chem. Chem. Phys.* **2014**, *16*, 17220 – 17230.
[37] M. Perfetti, *Coord. Chem. Rev.* **2017**, *348*, 171 – 186.
[38] S. Stoll, A. Schweiger, *J. Magn. Reson.* **2006**, *178*, 42 – 55.
[39] J. R. Pilbrow, *Transition Ion Electron Paramagnetic Resonance*, Clarendon Press, Oxford, UK, **1990**.
[40] J. S. Griffith, *The Theory of Transition Metal Ions*, University Press, Cambridge, UK, **1961**.
[41] F. Lloret, M. Julve, J. Cano, R. Ruiz-García, E. Pardo, *Inorg. Chim. Acta* **2008**, *361*, 3432 – 3445.
[42] A. V. Palii, D. V. Korchagin, E. A. Yureva, A. V. Akimov, E. Ya. Misochko, G. V. Shilov, A. D. Talantsev, R. B. Morgunov, S. M. Aldoshin, B. S. Tsukerblat, *Inorg. Chem.* **2016**, *55*, 9696 – 9706.
[43] A. Abragam, M. H. L. Pryce, *Proc. R. Soc. London Ser. A* **1951**, *206*, 173 – 191.
[44] a) K. S. Cole, R. H. Cole, *J. Chem. Phys.* **1941**, *9*, 341 – 352; b) C. Dekker, A. F. M. Arts, H. W. Wijn, A. J. van Duyneveldt, J. A. Mydosh, *Phys Rev. B* **1989**, *40*, 11243 – 11251.
[45] a) C. Plenk, J. Krause, E. Rentschler, *Eur. J. Inorg. Chem.* **2015**, 370 – 374; b) J. Palion-Gazda, T. Klemens, B. Machura, J. Vallejo, F. Lloret, M. Julve, *Dalton Trans.* **2015**, *44*, 2989 – 2992; c) X. Liu, L. Sun, H. Zhou, P. Cen, X. Jin, G. Xie, S. Chen, Q. Hu, *Inorg. Chem.* **2015**, *54*, 8884 – 8886; d) A. Świtlicka-Olszewska, J. Palion-Gazda, T. Klemens, B. Machura, J. Vallejo, J. Cano, F. Lloret, M. Julve, *Dalton Trans.* **2016**, *45*, 10181 – 10193; e) J. P. S. Walsh, G. Bowling, A.-M. Ariciu, N. F. M. Jailani, N. F. Chilton, P. G. Waddell, D. Collison, F. Tuna, L. J. Higham, *Magnetochem.* **2016**, *2*, 23 – 32.
[46] A. Lunghi, F. Totti, R. Sessoli, S. Sanvito, *Nat. Commun.* **2017**, *8*, 14620.
[47] A. Lunghi, F. Totti, S. Sanvito, R. Sessoli, *Chem. Sci.* **2017**, *8*, 6051 – 6059.
[48] A. Abragam, B. Bleaney, *Electron Paramagnetic Resonance of Transition Ions*, Dover Publications, Inc., Mineola, NY, **1986**.
[49] a) R. Ruamps, L. J. Batchelor, R. Guillot, G. Zakhia, A.-L. Barra, W. Wernsdorfer, N. Guihery, T. Mallah, *Chem. Sci.* **2014**, *5*, 3418 – 3426; b) S. Sottini, G. Poneti, S. Ciattini, N. Levesanos, E. Ferentinos, J. Krzystek, L. Sorace, P. Kyritsis, *Inorg. Chem.* **2016**, *55*, 9537 – 9548; c) M. A. Palacios, J. Nehrkorn, E. A. Suturina, E. Ruiz, S. Gomez-Coca, K. Holldack, A. Schnegg, J. Krzystek, J. M. Moreno, E. Colacio, *Chem. Eur. J.* **2017**, *23*, 11649 – 11661.
[50] Y.-Z. Zhang, S. Gómez-Coca, A. J. Brown, M. R. Saber, X. Zhang, K. R. Dunbar, *Chem. Sci.* **2016**, *7*, 6519 – 6527.
[51] F. Neese, *WIREs Comput. Mol. Sci.* **2012**, *2*, 73 – 78.
[52] a) G. Karlström, R. Lindh, P.-Å. Malmqvist, B. O. Roos, U. Ryde, V. Veryazov, P.-O. Widmark, M. Cossi, B. Schimmelpfennig, P. Neogrady, L. Seijo, *Comput. Mater. Sci.* **2003**, *28*, 222 – 239; b) V. Veryazov, P.-O. Widmark, L. Serrano-Andrés, R. Lindh, B. O. Roos, *Int. J. Quantum Chem.* **2004**, *100*, 626 – 635; c) F. Aquilante, L. De Vico, N. Ferré, G. Ghigo, P.-Å. Malmqvist, P. Neogrády, T. B. Pedersen, M. Pitoňák, M. Reiher, B. O. Roos, L. Serrano-Andrés, M. Urban, V. Veryazov, R. Lindh, *J. Comput. Chem.* **2010**, *31*, 224 – 247.
[53] S. Gomez-Coca, E. Cremades, N. Aliaga-Alcalde, E. Ruiz, *J. Am. Chem. Soc.* **2013**, *135*, 7010 – 7018.
[54] M. Atanasov, D. Ganyushin, K. Sivalingam, F. Neese in *Struct. Bond.* (Eds.: D. M. P. Mingos, P. Day, J. Peder), Springer, Berlin, **2012**, pp. 149 – 220.
[55] a) L. F. Chibotaru, L. Ungur, C. Aronica, H. Elmoll, G. Pillet, D. Luneau, *J. Am. Chem. Soc.* **2008**, *130*, 12445 – 12455; b) L. F. Chibotaru, L. Ungur, A. Soncini, *Angew. Chem. Int. Ed.* **2008**, *47*, 4126 – 4129; *Angew. Chem.* **2008**, *120*, 4194 – 4197.
[56] W. H. Harman, T. D. Harris, D. E. Freedman, H. Fong, A. Chang, J. D. Rinehart, A. Ozarowski, M. T. Sougrati, F. Grandjean, G. J. Long, J. R. Long, C. J. Chang, *J. Am. Chem. Soc.* **2010**, *132*, 18115 – 18126.

Manuscript received: February 28, 2018
Accepted manuscript online: April 14, 2018
Version of record online: May 30, 2018

